NPL
National Physical Laboratory

NPL REPORT MAT 92

INFLUENCE OF H_2S ON THE LOCALISED CORROSION OF 316L STAINLESS STEEL: PART 1 – COUPON TESTING

JAMES HESKETH, EDMUND J.F. DICKINSON, GREGORY MCMAHON, MAY MARTIN, ALAN TURNBULL AND GARETH HINDS

MAY 2020

INFLUENCE OF H_2S ON THE LOCALISED CORROSION OF 316L STAINLESS STEEL: PART 1 – COUPON TESTING

JAMES HESKETH, EDMUND DICKINSON, GREGORY MCMAHON, MAY MARTIN*, ALAN TURNBULL AND GARETH HINDS

Department of Electromagnetic and Electrochemical Technologies
* NIST, 325 Broadway, MS 647, Boulder, CO 80305

SUMMARY

Corrosion coupon immersion tests were performed on 316L SS in 50,000 ppm Cl^- at 110 °C to evaluate the effect of partial pressure of H_2S on pit depth and density in a simulated oilfield environment. The protective film formed in these environments was analysed by nanoSIMS and shown to consist of mixed metal sulphides and oxides, the former being considered to enhance chloride ion uptake leading to more ready passivity breakdown and pit initiation. H_2S is deduced to be acting primarily as a chemical agent in supporting subsequent pit propagation, adsorbing on the pit surface and constraining the repassivation process. Pitting was most severe at intermediate partial pressures of H_2S. At more elevated partial pressures, pitting was inhibited, which is attributed to blocking of the pit surface by dense sulphide phases that limited access of H_2S to the pit surface. Surface finish was shown to be a critical factor in pit development with specimens machine-ground to a Ra< 0.2 μm showing extensive pitting but with specimens hand-ground to a P1200 finish (Ra<0.1μm) showing very limited pitting.

ISSN 1754-2979

https://doi.org/10.47120/npl.MAT92

National Physical Laboratory
Hampton Road, Teddington, Middlesex, TW11 0LW

Approved on behalf of NPL by
Dr Fernando Castro, Head of Science, Department of Electromagnetic & Electrochemical Technologies

CONTENTS

1 INTRODUCTION

In the oil and gas industry, corrosion resistant alloy (CRA) pipelines are deployed for operating conditions considered too severe for application of carbon steel with chemical inhibition, or where the CRAs provide the most practical economic choice for system management. The environments tend to be mildly acidic, with a high concentration of chlorides, and contain H_2S. In combination with an elevated temperature, the conditions are highly corrosive and capable of inducing stress corrosion cracking (SCC). As such, materials that are specified must be shown to be resistant to SCC through laboratory qualification testing according to standards such as NACE MR0175/ISO 15156[1]. Tests for resistance to SCC typically involve exposing specimens of the stressed alloy to conditions broadly comparable or conservative to those encountered in service and performing post-test analysis to detect evidence of SCC.

The potential limitations of this approach are the relatively short timescale and small-scale nature of most testing, the idealised and variable surface preparation of test specimens in some cases, and uncertainty as to whether the laboratory environmental exposure conditions are sufficiently representative of service environments. While service experience of alloy performance can compensate to an extent, the complex interplay of variables such as salt composition and concentration, gas fugacity/pressure and composition, temperature, electrochemistry and stress mode, can challenge confidence in applying laboratory test data to materials selection and design for new, often more aggressive, oilfields. Confidence is undermined by the lack of fundamental understanding of the cracking mechanism and the relative significance of different variables in controlling the cracking process. The consequence can be over-conservatism and over-specification of material in design or, conversely and more concerningly, under-specification, resulting in catastrophic failure of in-service components. Improved understanding of the underlying mechanisms would lead to more reliable interpretation and application of test results, leading to reduced costs and safer operation.

In the presence of H_2S, the cracking mechanism can be complex. H_2S is often associated with stress corrosion cracking because of its ability to increase the uptake of hydrogen within a corroding material, as is the case for carbon and martensitic stainless steels. This is commonly referred to as sulphide stress corrosion cracking. However, for materials that are resistant to hydrogen embrittlement, such as stable austenitic stainless steels, the role of H_2S is more ambiguous. It can increase the tendency to cause corrosion pits, which act as initiation sites for cracks, but may also accelerate the stress corrosion cracking process itself – for example, by retardation of the oxide refilming process. For CRAs in oilfield environments, cracks are usually associated with corrosion pits, although that may not be exclusive. However, pits do not necessarily lead to the formation of cracks; whether they do so depends on pit size, pit geometry and pit growth rate. The associated uncertainty has resulted in a lack of guidance on the interpretation of observation from short-term tests for SCC of CRAs in which the material exhibits corrosion pits but without cracks. This has led to discussion of a threshold pit size for acceptance or rejection of a material but no consensus. In the absence of detailed insight, such a concept has been excluded from current standards and it is left to the end user to define their acceptance criteria.

To allow material selection decisions to be based on sound reasoning, better understanding of the pitting mechanism in sour conditions is required. Pitting has been studied in detail for many decades, yet most of the work has focused on marine environments. These conditions are very different to those encountered in sour oil and gas wells, which are essentially anoxic and contain hydrogen sulphide. As such, the well-developed, classical pitting models are not adequate to predict the response of alloys in these conditions and further insight is required.

This report describes Part 1 of a two-part study aimed at elucidating the role of H_2S in the pitting of 316L stainless steel (SS) in oil and gas brines.

- Part 1 explores the effect of bulk H_2S concentration and alloy surface preparation on the depth of corrosion pits that form under open circuit conditions.

- Part 2 explores the use of electrochemical testing to determine the influence of H_2S on the anodic and cathodic reaction kinetics.

2 MATERIAL CHARACTERISATION

All testing was performed on test specimens prepared from the mid-thickness of a 15 mm thick UNS S31603 (316L SS) plate, whose composition is shown in Table 1 (NPL material reference code – AFUQ). The alloy has an equiaxed austenitic grain structure with delta ferrite bands orientated in the rolling direction as shown in Figure 1. Identification of δ-ferrite was confirmed using scanning electron microscopy (SEM) and electron backscatter diffraction (EBSD), as shown in Figure 2.

Table 1: Composition of the 316L SS tested in this work (wt%) (AFUQ).

C	Si	Mn	P	S	Cr	Ni	Mo	N	Cu	Fe
0.015	0.43	1.28	0.030	0.002	16.75	10.07	2.05	0.043	0.41	Bal.

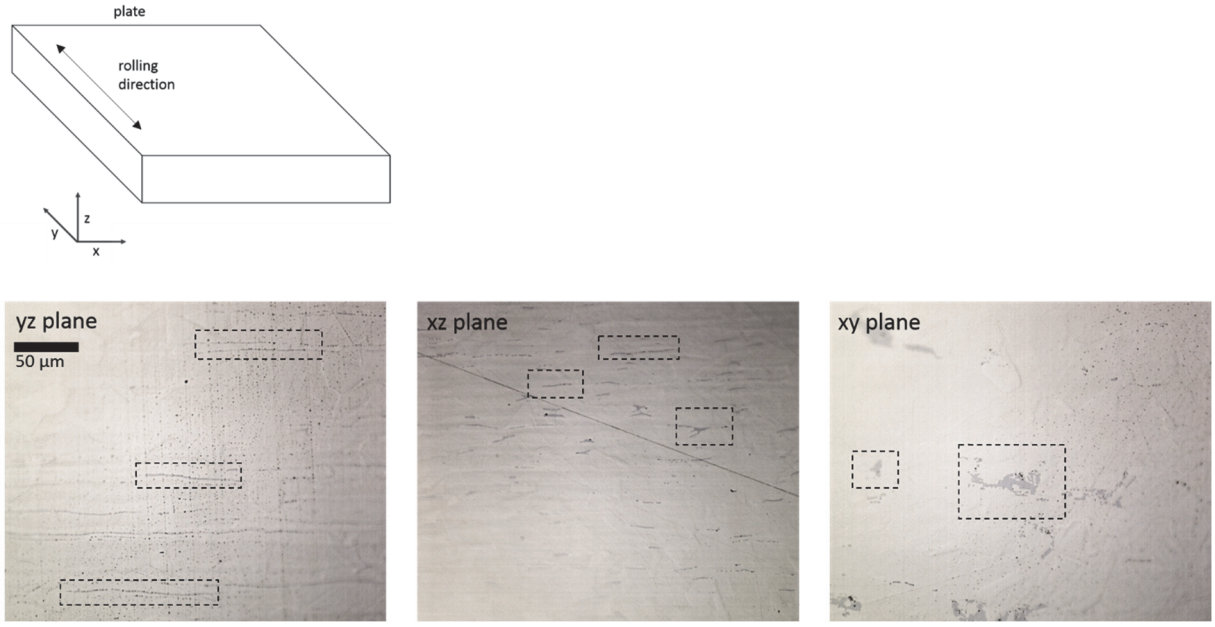

Figure 1: Optical micrograph showing AFUQ microstructure with bands of δ-ferrite highlighted.

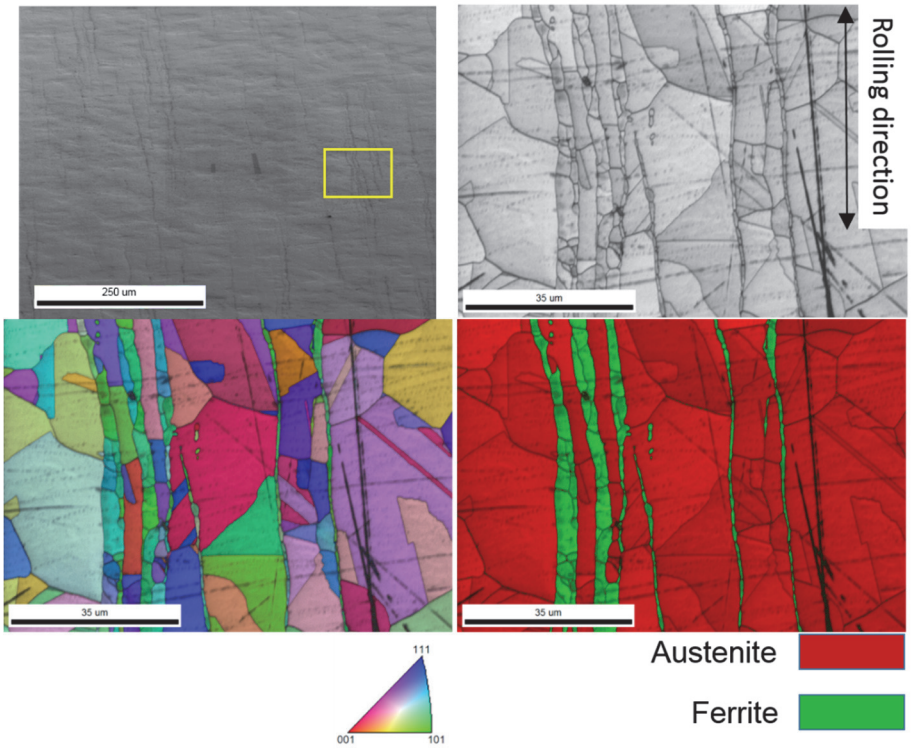

Figure 2: Electron micrographs showing microstructure of 316L SS used in this work; electron backscatter diffraction (EBSD) has been used to show grain orientation (bottom left) and phase (bottom right).

3 EXPERIMENTAL

3.1. OUTLINE

A series of corrosion coupon exposure tests was performed to investigate the impact of H_2S concentration on the propagation of corrosion pits on 316L SS. The experiment was designed to examine further the proposition that H_2S is consumed within a pit and repassivation occurs when the the H_2S that enters through the pit mouth is consumed before it reaches the active surface[2].

The conditions for the exposure tests were selected to be close to the pass/fail boundary with respect to resistance to SCC. The choice of exact solution chemistry required to achieve this was guided by previous studies on SCC of 316L SS in H_2S environments[3]. The first set of tests (Phase 1), was designed to allow measurement of the depth of pits that develop naturally in the absence of any applied electrochemical polarisation, but with varying H_2S concentration in the bulk solution. The main disadvantage is that analysis must be performed ex situ. Hence, no information regarding the time dependent initiation, growth and repassivation of pits can be obtained from a single experiment. To gain this information the second phase of the study was aimed at characterising the time dependence of pit depths. In this case, pitting tests were performed at a single concentration of H_2S for different periods of exposure.

3.2 PITTING CORROSION SPECIMENS

3.2.1 Phase One

The specimens used had dimensions of 30 mm × 30 mm × 6 mm and contained a 6 mm diameter hole drilled into the face for ease of suspension from a polytetrafluoroethylene (PTFE) sample holder (shown in Figure 3). The two large test surfaces of the specimen were prepared by first milling the surface of the supplied metal plate, then grinding a further 0.1 mm from each surface to achieve a finish of Ra ≤ 0.2 μm, compatible with NACE standards such as TM0316[4]. The deep surface grind was performed to remove the sub-surface material that had been deformed during the milling step. The sides of the specimen were ground to a similar nominal Ra value after cutting but without initial milling. Grinding of stainless steels has been shown to generate a surface nanocrystalline layer and subsurface plastic deformation with the depth dependent on the grinding procedure[3]. This is evidenced here also in Figure 4, which shows that the near-surface microstructure still exhibited grain refinement (reflected in non-indexable grains, consistent with a nano-size grain structure), residual plastic deformation and a high-density of slip bands. Nano-sized grains are expected with grinding; the concern is the extent of sub-surface deformation and slip that seems more representative of a machined surface.

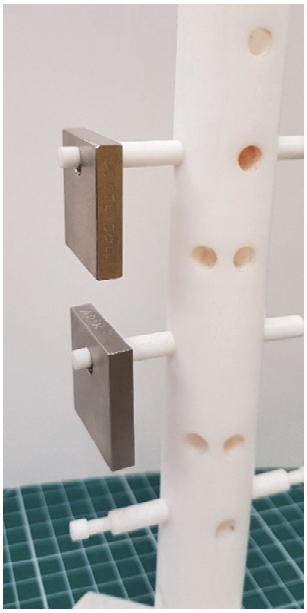

Figure 3: Corrosion coupon test specimens mounted on PTFE holder.

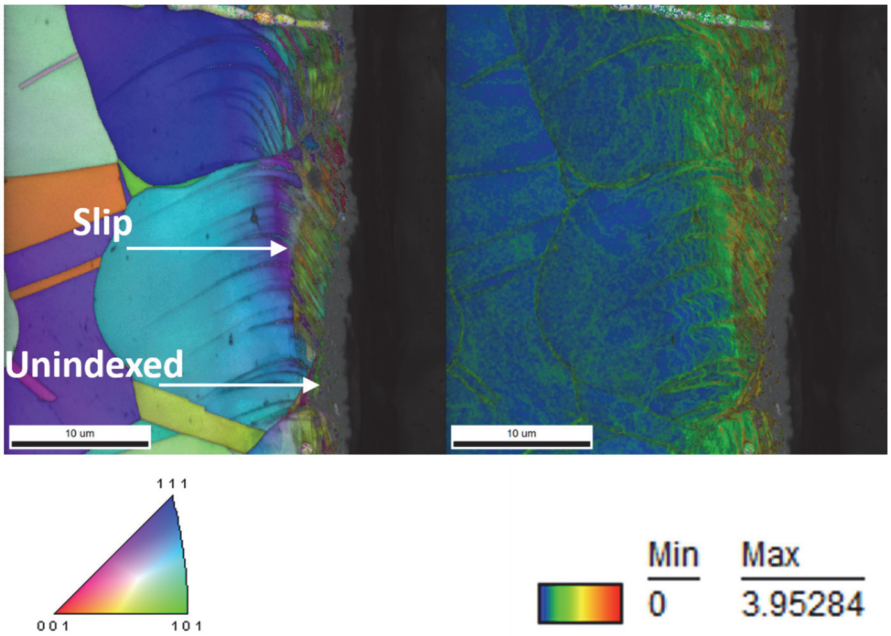

Figure 4: Transverse cross-section of untested pitting coupon specimen shown by EBSD orientation map (left) and EBSD grain reference orientation colour and map (right) superimposed on to grey scale image quality maps.

3.2.2 Phase Two

For the second phase of pitting tests, the preparation of the test coupons was modified to address some issues that presented themselves in Phase 1, and are discussed in more detail later. For Phase 2, the coupons were mounted in a chemically resistant resin so that only one face was exposed. This surface was then wet ground using P1200 SiC paper 24-72 hours prior to testing, which gives Ra < 0.1 μm. In order to evaluate the potential influence of microstructural orientation, coupons of two geometries were used, either 30 mm × 30 mm × 8 mm, or 30 mm × 8 mm × 8 mm. For the larger coupons, the surface that was exposed was one of the square 30 mm × 30 mm faces. For the smaller coupons, the face that was exposed was one of the rectangular 30 mm × 8 mm faces. Figure 5 shows the orientation of each of these coupons with respect to the rolling direction of the plate.

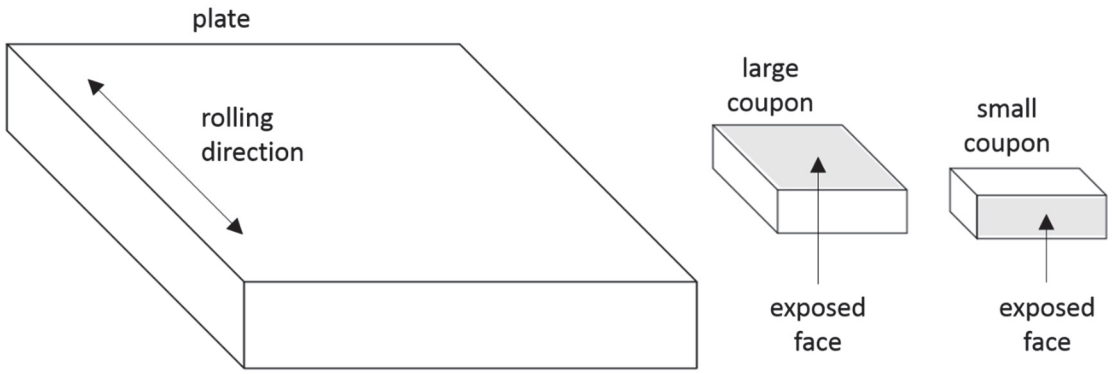

Figure 5: Orientation of test specimens with respect to the rolling direction of the plate.

3.3 PROCEDURE FOR PITTING CORROSION TESTS

3.3.1 Phase One

The autoclaves used in the pitting corrosion tests were configured as shown in Figure 6. Testing was conducted according to the following procedure.

Test solution was prepared to represent produced water with a chloride concentration of 50,000 ppm, at a temperature of 110 °C. At this level of chloride, 316L SS is resistant to SCC only at a higher pH and lower H_2S partial pressure (cf. condensed water with typically less than 1000 ppm Cl^-). In this case, test solutions were buffered to a pH of either 4.0 or 4.5 under a standard set of conditions (1 bar CO_2, ambient temperature) by addition of CH_3COONa + HCl , or $NaHCO_3$, respectively. Table 2 summarises the individual test conditions. The in situ pH and calculated buffering capacity at the in situ pH (defined as the differential addition of strong base required to vary the pH by one unit) of these two solutions are quoted, as calculated at the test temperature using MTDATA thermodynamic and phase equilibria software (Hampton Thermodynamics Ltd). From the table, the CH_3COONa + HCl buffer system gives pH values close to the nominal value across the range of H_2S partial pressures. In contrast, the $NaHCO_3$ containing solution has an *in situ* pH about 0.5 units greater than the nominal value. Furthermore, the buffering capacity of the CH_3COONa + HCl buffer remains consistent over the range of studied conditions, and is substantially greater than that of the $NaHCO_3$ containing solution, whose buffering capacity is mostly derived from the dissolved gases and hence varies depending on the partial pressures of H_2S and CO_2.

Table 2: Test conditions for the Phase 1 pitting corrosion tests.

Test #	pH_2S (bar)	pCO_2 (bar)	pH_{nom}	In situ pH*	$[H_2S_{(aq)}]$ (mM)*	Time (days)	Buffering capacity (mM)	$[Cl^-]$ (ppm)	T (°C)
1.1	0.0	1.000	4.5	4.94	0	30	0.0219	50000	110
1.2	0.010	0.990		4.93	0.22		0.0387		
1.3	0.050	0.950		4.90	1.19		0.105		
1.4	0.100	0.900		4.87	2.36		0.187		
1.5	0.250	0.750		4.78	5.82		0.362		
2.1	0.0	1.000	4.0	3.92	0	30	1.13	50000	110
2.2	0.001	0.999		3.92	0.02		1.13		
2.3	0.010	0.990		3.91	0.22		1.13		
2.4	0.050	0.950		3.91	1.10		1.14		
2.5	0.100	0.900		3.91	2.21		1.15		
2.6	0.250	0.750		3.90	5.52		1.18		
2.7	0.010	0.990		3.92	0.22	1	1.13		

** calculated from MTDATA (Hampton Thermodynamics Ltd.) and previous thermodynamic data*

The test procedural steps were as follows:

1. Test specimens were degreased in acetone, rinsed in isopropanol and dried in air.
2. The specimens were suspended from a PTFE stand and were placed into the autoclave.
3. Test solution, in a separate vessel, was deaerated using high-purity nitrogen (> 99.998%) to reduce the dissolved oxygen concentration to less than 10 ppb according to a previously validated procedure[5]. The flow of nitrogen was used to simultaneously deaerate the autoclave containing the test specimens.
4. The deaerated solution was introduced to the deaerated autoclave using nitrogen pressure, following which the solution was sparged with nitrogen for a further hour to mitigate against oxygen ingress that may have occurred during transfer of the solution between vessels.

5. The solution was then sparged with a certified mixture of CO_2 and H_2S at the desired H_2S/CO_2 partial pressures at a rate of 100 ml/min for a minimum of 1 hour per litre of test solution.
6. Autoclaves were heated, with the gas mixture still flowing, to a temperature of 57 °C, at which stage the gas flow through the submerged inlet was stopped as blockage by salt deposit would ensue.
7. The autoclave was then heated to 110 °C and the CO_2/H_2S gas mixture was introduced to the head space of the autoclave using an inlet tube not submerged in the solution, at 100 ml/min for 1 hour.
8. The inlet and outlet of the autoclave were sealed, and the test temperature was maintained to within ±0.5 °C for 30 days.
9. Upon completion of the test, the autoclave was vented and cooled back to ambient temperature then purged with high-purity nitrogen for 24 hours before it was opened to remove the test specimens.
10. Test specimens were chemically cleaned using 50% HCl + 10 g/L of dibutylthiourea and rinsed in deionised water to remove the pit corrosion products. For specimens examined by SEM, the chemical cleaning step was not performed, and pits were rinsed with deionised water only.
11. Test specimens were examined using an Alicona Infinite Focus confocal microscope (Alicona Imaging GmbH, Graz, Austria) to look for evidence of pitting corrosion. The maximum observable depth and diameter of the major and minor axis of the opening of each pit was measured and recorded.

All corrosion coupons were tested in duplicate.

It was decided to fill and seal the autoclaves as opposed to charging them with gas continuously so that multiple tests could be run simultaneously within NPL's H_2S laboratory. This method is suitable when testing CRAs as the expected rate of consumption of H_2S, through sulphide formation, is low and not anticipated to cause a significant depletion over the normal test duration of one month. Sparging the solution with the H_2S/CO_2 gas mixture prior to heating can introduce undesirable stress corrosion cracking (SCC) in alloys that are sensitive to SCC at temperatures below the test temperature and is advised against. In this work, where only pitting was investigated, it was adopted in order to avoid blockage of the gas inlet tube with salt, which occurs at higher temperatures even with humidified gas. However, when this is done with a mixture of two or more gases, the differential change in solubility of the gases can cause their relative partial pressures to change from that desired for the test. Step 7 is designed to prevent this by replenishing the headspace of the autoclave with the gas mixture in the correct stoichiometric ratio. If this is not done, then it is predicted, using MTDATA thermodynamic software, that the H_2S partial pressure could be up to 20%* greater than expected from its stoichiometric ratio in the gas mixture.

** calculated for a 50% full autoclave.*

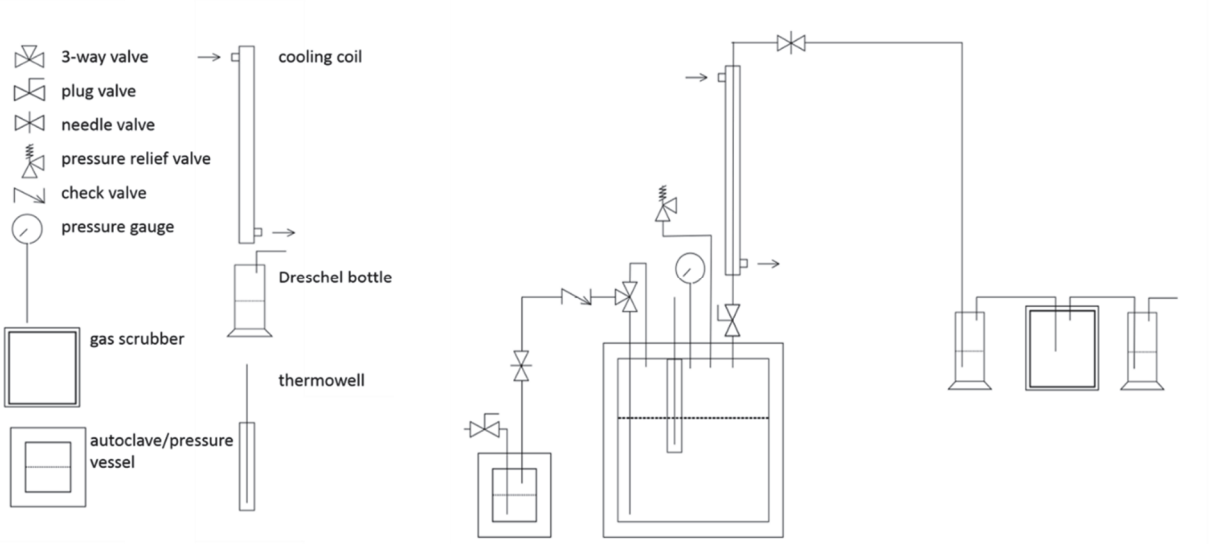

Figure 6: Autoclave configuration used for all tests at elevated temperature and pressure.

3.3.2 Phase Two

In Phase 2, the coupons were set in a chemically resistant 2-part epoxy coating (Masterbond EP62-1HT) that was cured at 100 °C for 30 minutes. Once cured, this coating provided an impermeable barrier to 5 of the 6 faces of the coupon. The remaining face was then wet ground using P1200 SiC paper 24-72 hours prior to testing. This was done to ensure that each specimen had a comparable surface in terms of oxide age, residual strain and roughness. During testing, it was noticed that the epoxy coating was very brittle and prone to breaking during assembly of the tests. To mitigate this, specimen holders were produced from polyvinylidene fluoride by additive manufacturing and the specimens were set into them using the same epoxy resin. This provided mechanical support for the resin and prevented it from breaking. As mentioned previously, two different geometries of specimen were tested whose exposed surface was at a different orientation with respect to the rolling direction of the plate material. This enabled assessment of the impact of microstructural orientation on pit propagation. In addition, tests were conducted in which a specimen of relatively low surface area was coupled to a specimen of larger surface area. The area ratio of the coupled coupons was 1:2.54.

For tests of a shorter duration, it was possible to perform electrochemical measurements in situ (although corrosion potential measurement was limited for longer test durations due to gradual contamination of the high-pressure reference electrode by H_2S). Electrical connections were made to these specimens by spot welding a nickel wire sheathed in polyetheretherketone (PEEK) to the back of the specimen and sealing the weld in epoxy. Measurement of the coupled potential and the galvanic current between the two coupled coupons was made using a potentiostat with an integrated zero-resistance ammeter (ZRA). The same procedure was then followed as described for the Phase 1 tests, except specimens were not suspended from PTFE stands but instead were placed face up on a PTFE sheet at the base of the autoclave. The test conditions are given in Table 3 and test solutions were produced as described for Phase 1.

Table 3: Test conditions for the Phase 2 pitting corrosion tests.

Test #	Time (days)	Test Specimens	pH_2S (bar)	pCO_2 (bar)	pH_{nom}	In situ pH*	$[H_2S_{(aq)}]$ (mM)*	Buffering Capacity (mM)	$[Cl^-]$ (ppm)	T (°C)
1	1	3 Small 3 Large 3 Coupled	0.01	0.99	4.0	3.91	0.22	1.13	50000	110
2	5	3 Small 3 Large 3 Coupled								
3	10	3 Small 3 Large								
4	15	3 Small 3 Large								
5	30	3 Small 3 Large								

** calculated from MTDATA (Hampton Thermodynamics) and previous thermodynamic data [5]*

Several small coupons were prepared for nano-Secondary Ion Mass Spectrometry (nanoSIMS) by polishing one of the faces to a mirror finish using colloidal silica. This fine surface finish is not representative of the surface condition in service or typical test specimens used for pitting and cracking studies but is necessary to obtain good quality nano-SIMS data. The highly polished surface is expected to confer superior pitting resistance on the specimen; hence, nano-SIMS was only used to provide general information regarding the composition of the surface film. Specimens were exposed for either 0 (unexposed control specimens), 5 or 10 days in the same autoclaves as the pitting specimens. Following testing, samples were cut from select coupons using a precision cutting wheel and were analysed using nanoSIMS.

NanoSIMS image depth profiles were performed on a Cameca NanoSIMS 50L instrument (Gennevilliers, France). A Cs^+ primary ion beam was used to sputter the sample and negative ions were detected. The impact energy of the primary ion beam was 16 keV/ion. The primary beam ion current measured by a Faraday cup in the primary column (Fcp) was 40-45 nA. The detectors were moved to the appropriate radii to detect ^{16}O (Detector 1), $^{12}C_2$ (Detector 2), ^{32}S (Detector 3), $^{32}S^1H$ (Detector 4), ^{35}Cl (Detector 5), ^{56}Fe (Detector 6) and $^{32}S^{16}O_2$ (Detector 7). Mass resolution was ~7000 measured at $^{12}C_2$ using a 30 µm width entrance slit (Es-3) and a 350 µm width aperture slit (As-1). Mass spectra were checked at each detector prior to each image acquisition and the deflection voltage at each detector was set to ensure only the desired mass was deflected through the exit slit to the detector.

Imaging was performed by rastering the ion beam across the sample surface with a 25 µm field of view without any form of pre-sputtering or implantation in order to preserve the surface layer(s) chemistry. The raster size in pixels was 256 × 256 and the primary beam dwell time was 2.5 µs/pixel. A primary ion beam aperture diameter of 150 µm was used (D1-4), which would enable a spot size of ~ 100 nm -150 nm. The process was repeated until the secondary ion signals reached a constant level indicating that all surface layers had been completely removed and analyzed and the bulk material had been reached. This typically resulted in image stacks containing 200-300 images.
Data was processed using the open source ImageJ [https://imagej.nih.gov/ij/] plugin OpenMIMS software [https://github.com/BWHCNI]. The image stacks were aligned to account for any stage drift during the analysis period. Regions of interest within obvious grains (demonstrated by crystallographic contrast in the secondary ion images) were drawn and the counts for all seven measured masses were extracted to form the depth profile data.

4 RESULTS

4.1 PITTING AS A FUNCTION OF H_2S CONCENTRATION (PHASE 1)

The results of the Phase 1 pitting corrosion tests performed in different concentrations of H_2S are given in Table 4. Features less than 10 µm in depth were ignored since untested specimens exhibited many pit-like defects of this scale. In general, the sides of the corrosion coupons appeared more susceptible to localised corrosion than the faces. Since the surface preparation and microstructural orientation are different for the sides and faces of the coupon, pit distributions have been analysed separately for each. Figure 7 and Figure 8 show the measured distribution of pit depths for the 30-day tests buffered to a pH_{nom} of 4.5 and 4.0 respectively. From the table and figures, it is evident that the relationship between the severity of pitting and the bulk concentration of H_2S is not simple. At both pH values, the greatest number of pits and the largest pits formed at intermediate H_2S concentrations. Furthermore, the test performed for just 1 day in pH_{nom} 4.0 brine with 0.01 bar H_2S exhibited a maximum pit depth comparable to that in the test performed in the same environment for 30 days, albeit with fewer pits observed. This suggests that either the pit growth rate was rapid initially, but the growth rate then declined significantly, or that the pit growth arrested completely prior to test termination.

Table 4: Number and depth of pits formed during pitting corrosion coupon tests performed in Phase 1. The area of the two faces is 1800 mm^2 and that of the sides is 720 mm^2.

Test Number	pH_2S (bar)	pH_{nom}	Test duration (days)	Total number of pits	Number of pits on faces	Number of pits on sides	Mean pit depth on faces (µm)	Mean pit depth on sides (µm)
1.1	0.0	4.5	30	3	3	0	13.7	0
1.2	0.010			51	43	8	13.8	15.1
1.3	0.050			20	7	13	17.6	31.6
1.4	0.100			31	22	9	22.9	23.6
1.5	0.250			33	15	18	16.8	25
2.1	0.0	4.0	30	17	17	0	21.6	0
2.2	0.001			16	16	0	14.1	0
2.3	0.010			48	6	42	23	84.1
2.4	0.050			76	2	74	32	39.3
2.5	0.100			10	4	6	31.5	21
2.6	0.250			16	0	16	0	18.6
2.7	0.010		1	6	0	6	0	78.8

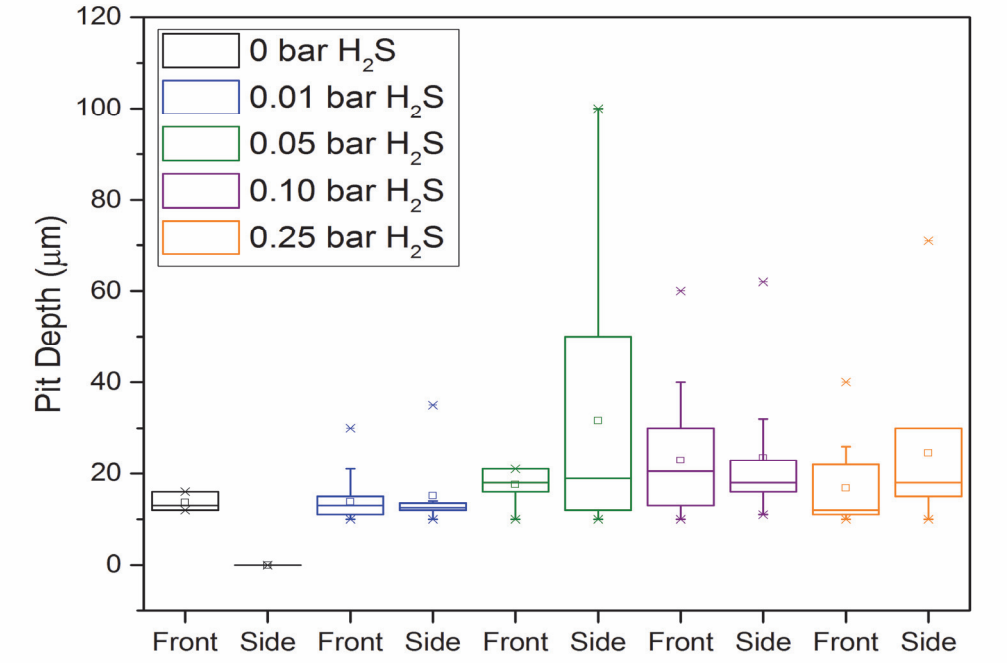

Figure 7: Distribution of pit depths across face and side of corrosion coupons tested for 30 days at pH 4.5_{nom}, 50,000 ppm Cl^-, 110 °C under different H_2S partial pressures at a total pressure of 1 bar (balance CO_2). Range is indicated by the stars, square box indicates the mean, the box indicates the median and quartiles whist the vertical lines indicate the 10^{th} to 90^{th} percentiles.

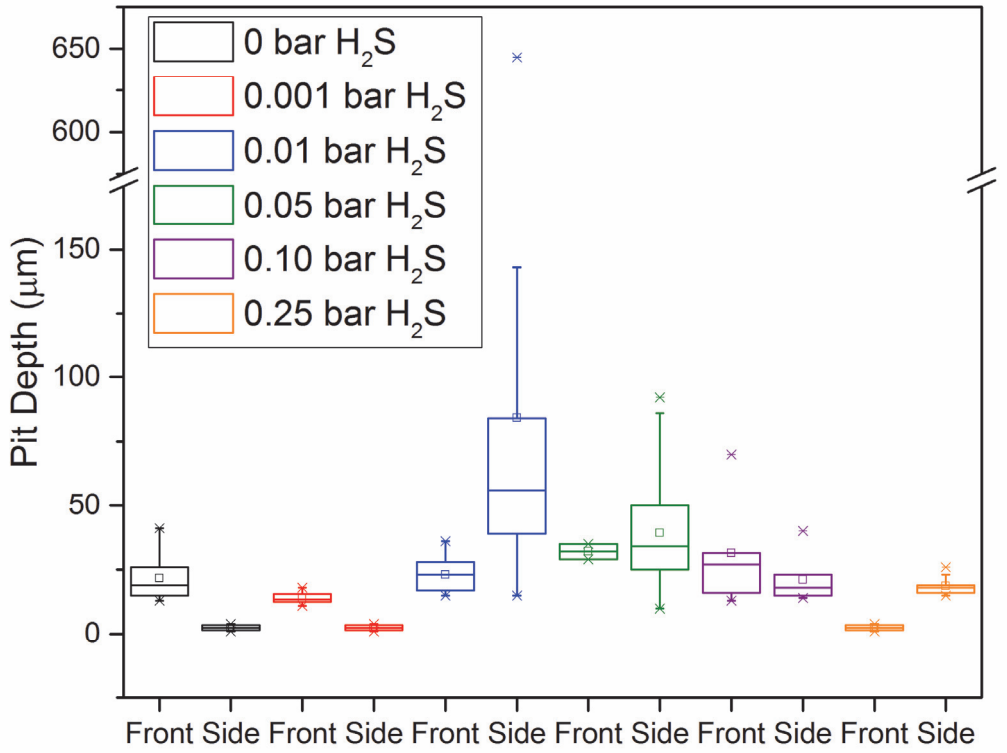

Figure 8: Distribution of pit depths across face and side of corrosion coupons tested for 30 day at pH 4.0_{nom}, 50,000 ppm Cl^-, 110 °C under different H_2S partial pressures at a total pressure of 1 bar (balance CO_2). Range is indicated by the stars, square box indicates the mean, the box indicates the median and quartiles whist the vertical lines indicate the 10^{th} to 90^{th} percentiles. Note the break in ordinate.

Visual inspection of the pits following testing revealed that they contained large amounts of black corrosion deposit. The nature of this deposit was investigated using SEM and energy dispersive X-ray (EDX) spectroscopy to map the cross-section of selected corrosion pits. Figure 9 shows an SEM image of the cross-section of a corrosion pit, formed on the side of a coupon tested in 0.01 bar H_2S at pH 4.0. The pits are typically quite open, as compared to the transport-constrained bulbous shape typical of pitting of stainless steel in aerated chloride environments. In addition, more accurate EDX point scans were taken at several locations as shown in Figure 10 and used for elemental quantification, the results of which are given in Table 5. The presence of stringers in the bulk matrix can clearly be observed from the EDX maps which show an abundance of Cr and a depletion of Ni. The precipitate within the pit was predominately a mixture of chromium, oxygen, nickel and sulphur, with a strong overlap between the nickel and sulphur signal and a strong overlap between the chromium and oxygen signal, suggesting the presence of nickel sulphide and chromium oxide. Iron was also detected suggesting the presence of iron oxide/sulphide. In principle, the species solubility and precipitate composition could be affected by the cooling to ambient temperature. However, the pit size response to H_2S partial pressure makes it far more likely that the precipitation was significant at test temperature. The SEM image shows the presence of un-corroded stringers running top to bottom throughout the pit. Selective area electron diffraction (SAED) was performed on a TEM slide fabricated from one of the stringers and confirmed that it had a BCC structure, consistent with it being δ-ferrite (Figure 11). The chemical composition across the pit and surrounding area was mapped using EDX as shown in Figure 9.

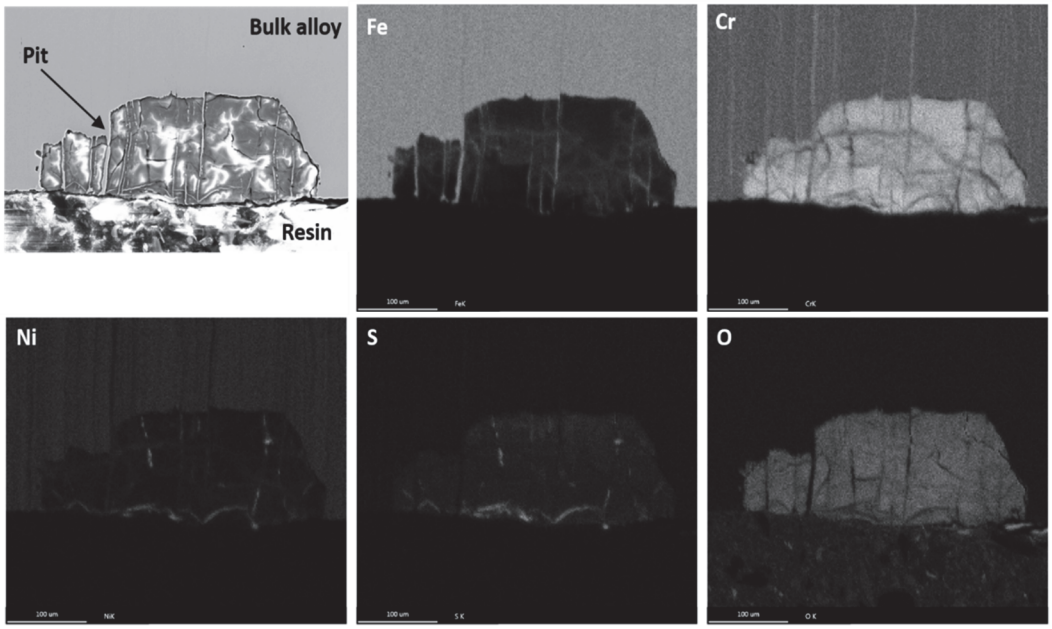

Figure 9: SEM image of corrosion pit cross-section (top left), and corresponding EDX elemental maps. The pit was formed in 0.01 bar H_2S, pH 4.0, 50,000 ppm Cl^-, 110 °C and formed on the side of the test specimen.

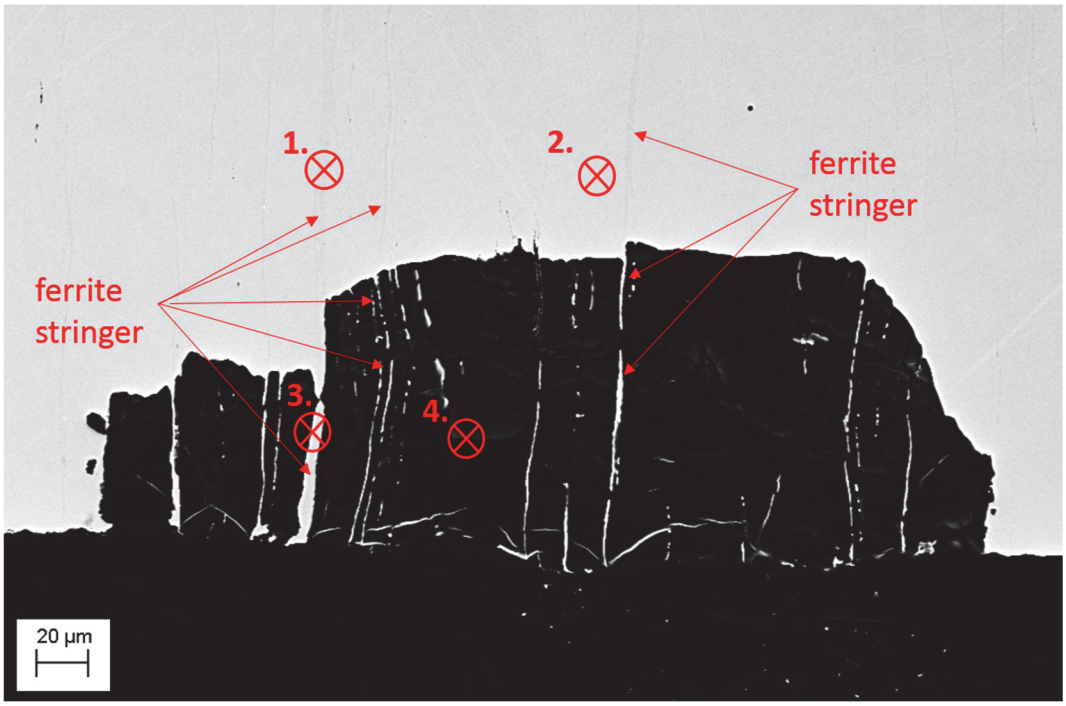

Figure 10: Backscattered electron image of a pit cross-section highlighting locations where quantitative EDX point scans were made. The pit was formed in 0.01 bar H_2S, pH 4.0_{nom}, 50,000 ppm Cl^-, 110 °C and formed on the side of the test specimen.

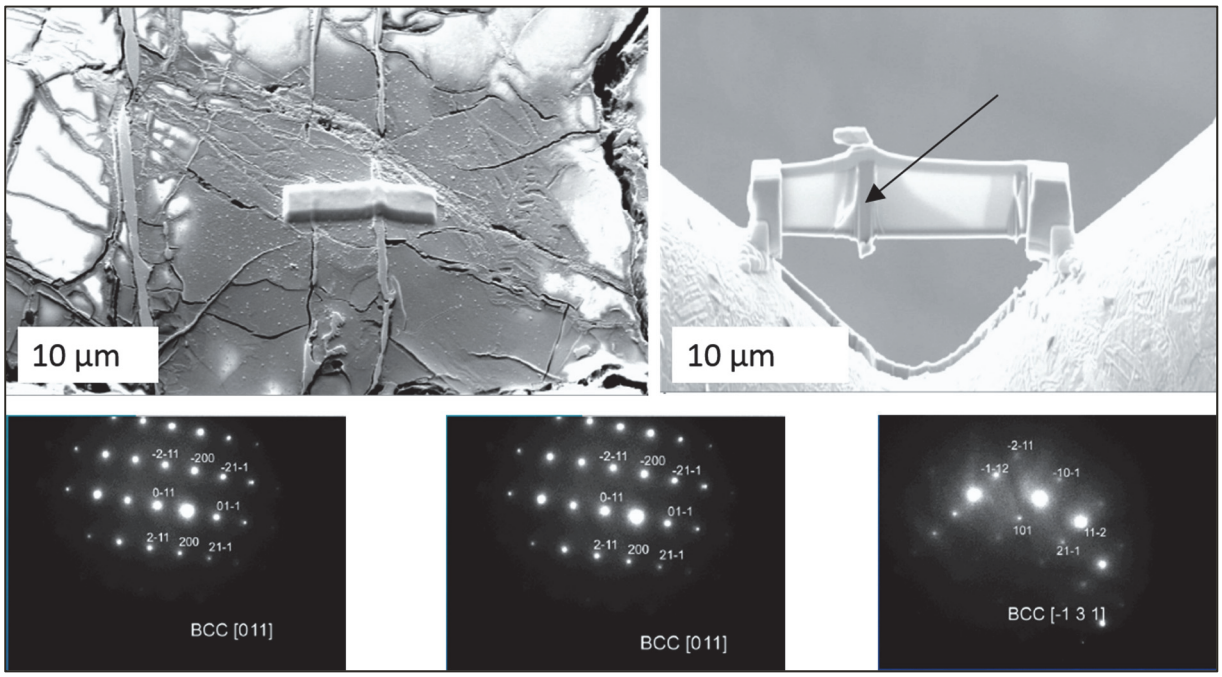

Figure 11: TEM slide preparation by focused ion beam SEM (top left), TEM slide containing stringer (top right), SAED patterns taken from stringer (bottom).

Table 5: SEM-EDX quantification from point scans taken as shown in Figure 10.

Area	Description	Cr	Fe	O	S	Mn	Mo	Ni
material spec.	bulk	16.8	69			1.3	2.0	10.0
1	ferrite in bulk	25.5	67.5			1.9	1.4	3.6
2	bulk	17.8	72.9				0.4	9.0
3	ferrite in pit	26.3	67.9			1.1	1.0	3.8
4	deposit in pit	49.5	29.9	13.6	3.0	0.8		3.2

Figure 12 shows a typical pit that formed on the face of a coupon. Here, there was no evidence of delta ferrite due to the orientation of the pit relative to the rolling direction. However, the pattern of corrosion at the base of the pit, with relatively sharp features evident, suggests possible preferential attack, perhaps at grain boundaries. Note that these images were based on pits that had not been chemically cleaned and the granular features inside the pits are associated with deposits.

.

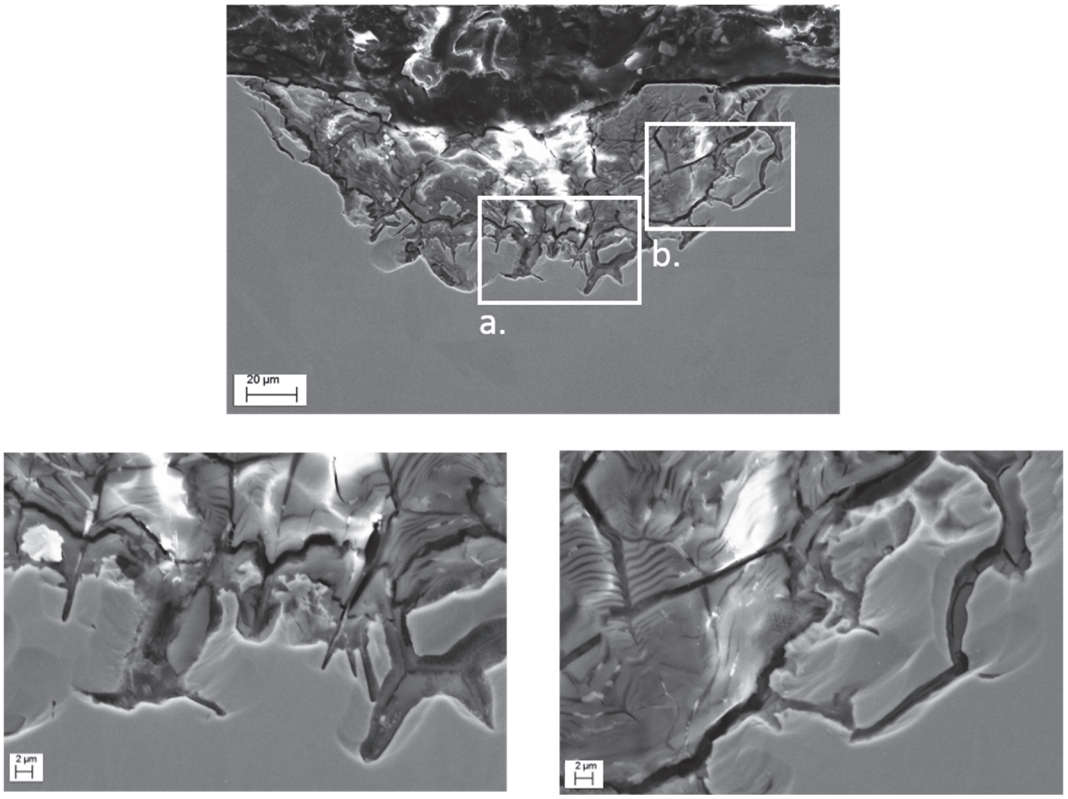

Figure 12: SEM image of a pit cross-section prior to cleaning, with enlarged regions a. (bottom left) and b. (bottom right). The pit was formed in 0.01 bar H_2S, pH 4.0_{nom}, 50,000 ppm Cl^-, 110 °C and formed on the side of the test specimen.

4.2 PITTING AS A FUNCTION OF TIME (PHASE 2)

4.2.1 Individual coupon immersion tests

The results of the pitting tests in Phase 2, performed at a H_2S partial pressure of 0.01 bar for different durations, are summarised in

Table 6 and plotted in Figure 13. Since the test specimens were ground to P1200 before testing, they typically had smaller surface defects and fewer of them compared to those used in Phase 1. Consequently, the threshold size for detection of pitting was reduced, and pits as small as 1 µm in depth could be readily identified. In general, the pits were considerably smaller than those measured during Phase 1. There was no consistent relationship between pit size and test duration, or between number of pits and test duration. Unlike in Phase 1, the orientation of the microstructure did not impact the pit depth. There was no clear systematic difference in the depth of pits of the small and large coupons despite their different orientation with respect to the plate (perpendicular for the small test coupon and parallel for the large coupon). This was unexpected given the strong influence of microstructural orientation observed in Phase 1 and may be related to the reduced size and number of pits that formed.

Table 6: Number and depth of pits formed during pitting corrosion coupon tests performed in Phase 2.

Test Number	Time (days)	Test Specimens	Pit density of large coupons (Pits/cm^2)	Pit density of small coupons (Pits/cm^2)	Mean pit depth on large coupons (µm)	Mean pit depth on small coupons (µm)
1	1	3 Small 3 Large	0.25	0	3.6	N/A
2	5	3 Small 3 Large 3 Coupled	0.94	0.28	7.1	5.5
3	10	3 Small 3 Large	1.38	0.551	4.7	3.3
4	15	3 Small 3 Large	2.25	1.29	6.4	6.2
5	30	3 Small 3 Large	0.40	0.09	6.7	11.3

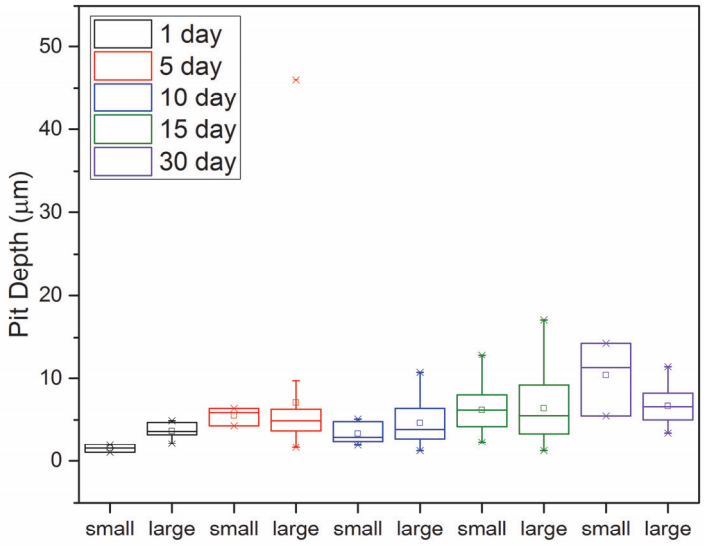

Figure 13: Distribution of pits across small and large coupons tested at pH 4.0$_{nom}$, 50,000 ppm Cl^-, 110 °C, 0.01 bar H_2S for different durations.

4.2.2 Coupled coupon tests

The coupled potential and galvanic current measurements for the three pairs of coupled coupons are shown in Figure 14.

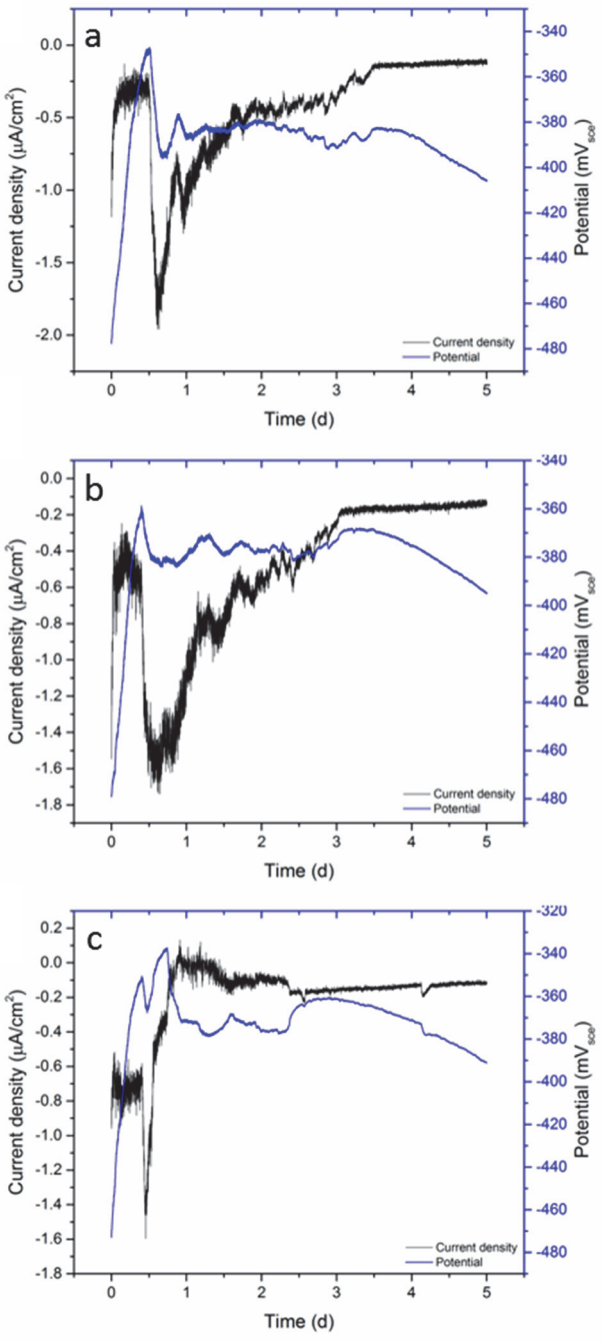

Figure 14: Coupled potential and galvanic current density between 3 separate pairs of coupled small and large coupons tested at pH 4.0_{nom}, 50,000 ppm Cl^-, 110 °C, 0.01 bar H_2S. Current density is defined with respect to the area of the smaller coupon as the current was flowing from the small electrode to the large electrode.

The negative current indicates that for each pair of coupons the larger coupon was the cathode and the smaller coupon was the anode. In each case, a positive shift in coupled potential of approximately

100 mV, from an initial potential of about -480 mV_{SCE}, occurred within the first day. For all three coupled coupons a sharp increase in the magnitude of the galvanic current density to 1 $\mu A/cm^2$ - 2 $\mu A/cm^2$ occurred with a corresponding dip in the coupled potential. Following this, the magnitude of the galvanic current declined; sharply in the case of the 3rd couple, but more slowly for couples 1 and 2. Inspection of the coupled coupons after testing revealed a few small pits 4 μm - 9 μm in depth and some crevice corrosion 8 μm - 78 μm in depth on each of the 3 smaller coupons. Two of the larger coupons also exhibited some small 4 μm - 10 μm deep pits but no crevice corrosion. The third coupled pair of coupons (Figure 14C) exhibited no pits on the larger coupon and just a single 2 μm pit and crevice corrosion 8 μm in depth on the smaller coupon. Crevice corrosion is undesirable as it can inhibit pit formation and invalidate the test; however, no crevice corrosion was observed on the individual uncoupled specimens that were used to obtain the pit sizes shown in Figure 13.

Applying Faraday's law of electrolysis to the total charge passage associated with this current flow enables the difference in total amount of metal dissolution between each coupon in the couple to be calculated. The difference in metal loss calculated between the two coupon is compared with extent of localised corrosion (pits and crevices) observed on each of the two coupons as shown in Table 7. From the table, it follows that the mass associated with the galvanic current flow between the coupled coupons is significantly greater than the estimated difference in mass loss associated with pits and crevices. This implies that that the galvanic current flow was mainly associated with imbalance of passive dissolution rate on the two specimens. Although crevice corrosion at the epoxy boundary was observed, the pit size in those regions was also determined and is included in the estimated mass loss for pits in Table 7. It is clear from the table that it would take the formation of a very large pit or crevice to shift the coupled potential of the two coupons significantly. This implies that the extent of the crevice corrosion that was observed did not inhibit the formation of corrosion pits and did not cause the oscillations in either the coupled potential or galvanic current between the coupled coupons.

Table 7: Comparison of the extent of localised corrosion and the mass loss associated with the galvanic current flow between coupled coupons.

	Estimated* mass loss associated with localised corrosion on the large coupon (μg)	Estimated* mass loss associated with localised corrosion on the small coupon (μg)	Mass associated with total galvanic charge (μg)	Total galvanic charge expressed as a single hemispherical pit diameter (μm)
Coupon pair 1	0.0142	13.9	128	1828
Coupon pair 2	0.0146	2.7	152	1936
Coupon pair 3	0	0.0076	62	1435

**assuming hemispherical shape*

4.3.3 NanoSIMS measurements

A representative sample of the nanoSIMS data for two regions of interest on the control specimen (see Figure 15) is given in Figure 16. It is evident that even in the absence of exposure to the test solution there was a degree of contamination of the surface by some of the species of interest, such as sulphur and chlorine. SIMS is a very sensitive surface analysis technique and can detect concentrations of species in the order of ppm to ppb. As such, measurement of some level of contamination is expected, and the results do not reflect a shortcoming in the procedure used to prepare or store the specimens. Each of the regions of interest of the control specimen yielded the same basic trend. The dominant species detected was oxygen (^{16}O), which showed an increase in concentration with time to a peak value followed by a steep decline to a steady state value. The steady state oxygen concentration indicates that the ion beam had penetrated to the bulk material at which point the oxygen signal is attributable to contamination within the instrument, further highlighting the sensitivity of the measurement. The next strongest signal was from sulphur (^{32}S), which showed the same basic trend as

the oxygen profile, but the signal tended to zero as opposed a to a steady state value. This indicates that the oxide film on the surface of the specimen contained some sulphur despite not being exposed to H_2S. Because the sensitivity of nano-SIMS is ion specific, the relative magnitude of the oxygen and sulphur signal cannot be used to determine the composition of the surface. The technique is extremely sensitive to sulphur; hence, a strong sulphur signal may only indicate a trace concentration. The third strongest signal was from carbon ($^{12}C_2$), which exhibited a peak value at a slightly shallower depth than the oxygen and sulphur. This then decayed to zero at a depth slightly below that of the oxide. This likely indicates the presence of some organic carbon contamination within the film and is not attributable to the carbon that is present in solid solution, which does not contribute to the $^{12}C_2$ signal. The chlorine (^{35}Cl) signal showed a very small peak within the upper layer of the oxide, which then decayed to zero. The $^{32}S^{16}O_2$ and $^{32}S^{1}H$ signals also exhibited very remote peaks in a similar position to that of the chlorine, whilst the signal from iron (^{56}Fe) was barely detectable at the very surface but showed a steep rise to a steady state value, indicating the ion beam had reached the base metal. The steady state ^{56}Fe signal was very weak, despite being a major species in the bulk and again demonstrates the ion specific sensitivity of the nanoSIMS technique.

The measurements taken from four regions of interest (Figure 17) of the specimens that had been exposed to the sour environment for 10 days all showed the same general trend (Figure 18). Like the control specimen, oxygen gave the strongest signal, which rose to a rapid peak with time then decayed to a steady state value, where the steady state value indicates the signal attributable to contamination within the instrument. Compared with the control sample the background oxygen signal was roughly the same, but the peak was much greater, indicating a higher density of oxygen within the surface film. The next strongest signals were measured for chlorine and sulphur, whose signal showed the same general shape as the control specimens but was considerably stronger, indicating a much greater amount of both chlorine and sulphur present in the film. The iron signal showed a small peak before reaching a steady state value, which may indicate an increased concentration of iron oxide or iron sulphide present in the inner layer of the surface film. It also took a greater amount of time to reach a steady state iron signal, which implies that the surface film was thicker overall. Exposure to the test environment did not affect the carbon signal, which showed evidence of a small amount of carbon contamination at the surface and may be attributable to the organic solvents used to degrease the specimen prior to testing. The $^{32}S^{16}O_2$ and $^{32}S^{1}H$ signals showed a similar trend as observed for the control specimen but with slightly higher peak signals, indicating a higher density of sulphur species present in the film, which is consistent with the increased (^{32}S) signal.

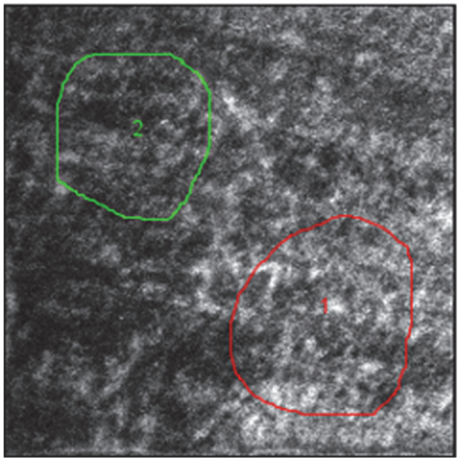

Figure 15: Electron micrograph of 316L SS control specimen showing two regions of interest that were analysed using nanoSIMS.

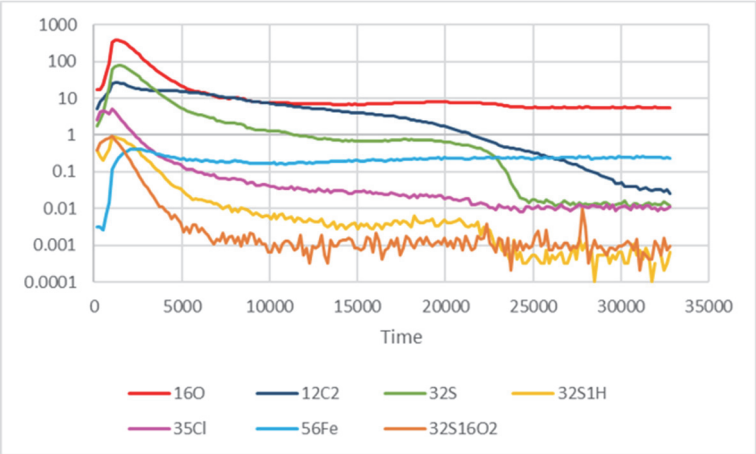

Figure 16: NanoSIMS measurements taken from region of interest 1 of control specimen shown in Figure 15.

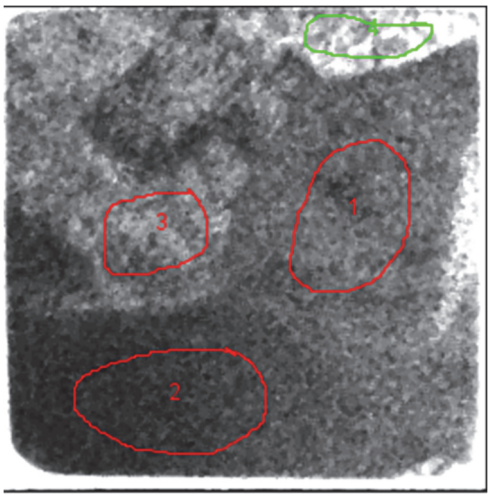

Figure 17: Electron micrograph of 316L SS specimen exposed to 0.01 bar H_2S, 110 °C, 50,000 ppm Cl^- at pH 4.0 for 10 days, showing four regions of interest that were analysed using nanoSIMS.

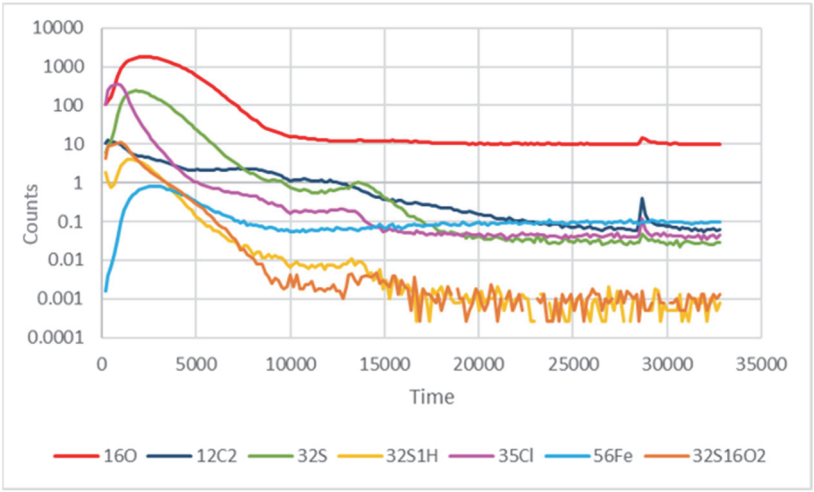

Figure 18: NanoSIMS measurements taken from region of interest 1 of the specimen shown in Figure 17.

5 DISCUSSION

5.1 PITTING CORROSION IN ANOXIC SOLUTIONS CONTAINING H_2S

In *aerated* chloride solution, passivity breakdown of stainless steel is known to initiate in a highly localised manner. The detailed mechanism of this initiation continues to be debated, depending on whether the role of chloride is perceived to undermine the passive film by some mechanism or to stabilise corrosion at natural dynamic breaks in the film. The presence of surface defects and inclusions also impacts on the site of initiation and early pit development and must be factored into any proposed mechanism of pit evolution. The role of surface defects is often overlooked, yet may be of greatest significance for surface conditions relevant to service. The metastable micropits that form upon film breakdown will develop into stable pits only if the dissolution current is able to sustain a local chemistry in the micropit sufficient to prevent repassivation and maintain the surface in the active state. That local chemistry, for the aerated solution case, is characterised by local depletion of oxygen and a concentrated metal salt solution greater than 55% of the saturation concentration[6,7]. The pH will decrease in response to hydrolysis of metal ions and to the increased ionic strength of the concentrated metal salt solution, with pH values typically between 0 and 3 for austenitic stainless steels[7]. Oxygen reduction external to the pit will continue to drive the dissolution current in the pit in the form of a differential aeration cell but with reduction of hydrogen ions in the low pH solution within the pit limiting the decrease in pH to some extent. In essence, the onset of the additional anodic current in the pit must be balanced by a corresponding increase in the cathodic current. This is achieved by a negative shift in the mixed potential, which will increase the cathodic current and also lead to a slight decrease in the anodic current in the pit. Clearly, if there are multiple pits there will be competition for available cathodic current and average pit growth rates will decrease.

The understanding of pitting of stainless steel in anoxic solutions is less well developed. It is well established that exposure of stainless steel to H_2S results in sulphide integration within the passive film[8, 9] and decreases passivity in the presence of chlorides[10-13]. The indication is that the passive current density would be increased relative to the H_2S-free solution, although comparative data at long duration are not available. The nanoSIMS measurements in the present study indicate that exposure to H_2S-saturated brine led to a high uptake of both sulphide and chloride into the oxide layer. Whilst the exact consequence of the presence of sulphides is not clear due to their protective effects in some cases[11, 14-16], chloride is well known to severely affect the pitting resistance of stainless steel[17-21]. As proposed previously[22], sulphide and chloride in the film may act synergistically, whereby the integration of sulphide into the passive film facilitates further infiltration by chloride. This would explain the more ready breakdown of the passive film.

Whilst the factors affecting initiation are progressively becoming clearer, the key role of H_2S in propagation of pits in stainless steels is less well defined. The free corrosion potential in mildly acidic environments of pH 4 or above can be several hundred mV more negative than that for aerated solution. By implication, the electrochemical driving force for the dissolution reaction is reduced relative to aerated solution while that for cathodic reduction is increased. Despite the lower corrosion potential of 316L SS in these oxygen-free acidic solutions, which would otherwise make pit propagation unsustainable, the potential is not low enough to suppress the tendency for pitting in the presence of H_2S. Electrochemical measurements[23] do not support the role of H_2S as a significant cathodic reactant in acidic environments of relevance to this study, although more recent cathodic polarisation measurements suggest a greater complexity than this simple statement might imply[24].

The main uncertainty is the chemistry within the pit under these exposure conditions and the role of H_2S in maintaining activity. By implication of the electrochemical measurement, H_2S is acting principally as a chemical agent. In oilfield brines[16], the depassivation pH of duplex stainless steel was observed to increase from 1.2 in sweet conditions to 2.2 and 3.2 at H_2S partial pressures of 0.01 bar and 1 bar, respectively[11, 16]. The depassivation pH measured in these tests does not necessarily correlate directly with the repassivation pH; nevertheless, by implication, in the presence of H_2S, it may be possible for pit growth to be sustained in a pit chemistry significantly less acidic than in

aerated solution. It raises the question of the extent of the acidity in the pit solution and the process by which H_2S undermines repassivation.

H_2S is a weak buffer that through dissociation restrains an increase in pH.

$$H_2S \rightleftharpoons HS^- + H^+ \qquad \text{Equation 1.}$$

However, in the experimental testing reported herein, buffering is also provided by acetate ions (pH 4 tests) and bicarbonate ions. Acetate ions will tend to resist a decrease in pH. Both ions will also preferentially migrate into the pit (compared to the neutral H_2S molecule) to balance the charge associated with the dissolving metal ions. Hence, the role of H_2S as a buffer in the pit may not be significant.

The hydrogen ion reduction reaction is very efficient in removing hydrogen ions, as one hydrogen ion is consumed per electron. However, the generation of hydrogen ions is less efficient as it involves first a metal ion dissolution process and then a subsequent weakly acidic hydrolysis reaction; i.e. one electron released in anodic dissolution does not generate one hydrogen ion. Hence, to achieve a reduction in pH in the pit solution, the dissolution current density must be much greater than the hydrogen ion reduction current density in the local pit solution. With the potential significantly lower than for aerated solutions, with relatively reduced dissolution kinetics, and enhanced hydrogen ion reduction, very low pH values typical of 316L SS in aerated chloride solution are not to be expected. Nevertheless, the steel is in the active state at a large overpotential with respect to the film-free state so the dissolution rate can be significant, as noted also in the lead-in-pencil experiments described in Part 2 of this report[24]. Previous experiments performed on various Ni/Cr/Mo alloys at 80 °C, 3.5% NaCl and 1 bar H_2S showed that even in anoxic conditions, the difference in the active and passive potential for this alloy was ~300 mV. However, it is evident from the limited pit depths observed that these proposed current densities must be short-lived, either because the pit dies or there is some constraint to growth.

Postulating a value for the likely pit solution pH in a complex test environment in the absence of modelling or experimental measurement would not be productive at this stage despite its importance. It is a component of a more complex chemistry that requires factoring in with a specific role for H_2S in the pit propagation process. The most likely mechanism for the latter, as proposed by Newman et al.[2], is that sulphur species adsorbed on the pit surface sustain activity and retard repassivation. What is less clear is the specific pit chemistry required to sustain the steel in the active state as a function of pit size, mixed potential and H_2S concentration.

There has to be a sustained supply of H_2S to that active pit surface, but this can be constrained by consumption of H_2S through metal sulphide formation. While H_2S can dissociate in the buffering process in response to hydrogen ion reduction, the maintenance of acidity through dissolution and hydrolysis will limit net consumption by that route unless the pH were to increase with changing pit depth. Accordingly, the limiting factor in supplying H_2S to the active pit surface will be reaction with metal ions to form the sulphide. That sulphide will effectively lock up the freely available H_2S for adsorption, the amount of freely available H_2S being then a balance of diffusion and reaction. With increasing pit depth that balance can change, and retardation of growth rate would follow. Increasing the concentration of H_2S might then be expected to increase the availability of H_2S, and, in simple terms, lead to an increased pit growth rate. However, this ignores the impact of the precipitation process on reaction kinetics on the surface.

The precipitation of metal sulphide within a pit is governed by the local metal ion concentration, the pH and the concentration of H_2S. This is shown in Equation 2, which describes the precipitation of FeS as an example. Given that a pit will invariably contain a high local concentration of metal ions, the precipitation of sulphide at a given pH is governed by the local H_2S concentration, whereby any H_2S over the solubility limit will react to form a precipitate. Precipitation of less soluble sulphides

such as those of molybdenum and nickel exhibit comparable behaviour, but in the absence of freely available data, FeS is given as the example.

$$c_{Fe^{2+}} = c_{Fe,crit,FeS} = \frac{K_{sp,FeS}}{c_{H_2S}} c_{H^+}^2 \quad \text{Equation 2.}$$

where $c_{Fe,crit,FeS}$ is the critical Fe^{2+} concentration for the onset of precipitation of H_2S as FeS, $K_{sp,FeS}$ is the solubility constant for FeS vs H_2S concentration and is taken as ~471.72 [25], c_{H+} is the concentration of H^+, and c_{H2S} is the concentration of H_2S in the bulk solution.

The concentration of Fe^{2+} required to precipitate FeS for a given pH has been plotted for the concentrations of H_2S associated with the partial pressure used in the Phase 1 pitting tests at pH_{nom} 4.0 (Figure 19). The solubility of FeS increases markedly with decreasing pH. High concentrations of dissolved metal ions are compatible with freely available H_2S for adsorption are attainable at low H_2S partial pressures but, of course, the unperturbed concentration of H_2S is small in these cases. What is not clear is whether a monolayer of adsorbed H_2S is sufficient, and, provided there is some H_2S available, active dissolution is maintained with a rate independent of H_2S concentration. At the higher H_2S partial pressures (0.10 bar and 0.25 bar), precipitation is expected at Fe^{2+} concentrations well below 1 M.

For a given concentration of metal ions, the precipitation of metal sulphide within a pit imposes a maximum limit on the concentration of dissolved H_2S. Hence, at higher bulk H_2S concentrations, the amount of precipitation that will occur within a given pit volume is greater, which increases the density of the precipitate. Lower density precipitates will be inherently more porous and less able to block mass transport, which may explain inhibition of pitting observed at higher concentrations of H_2S.

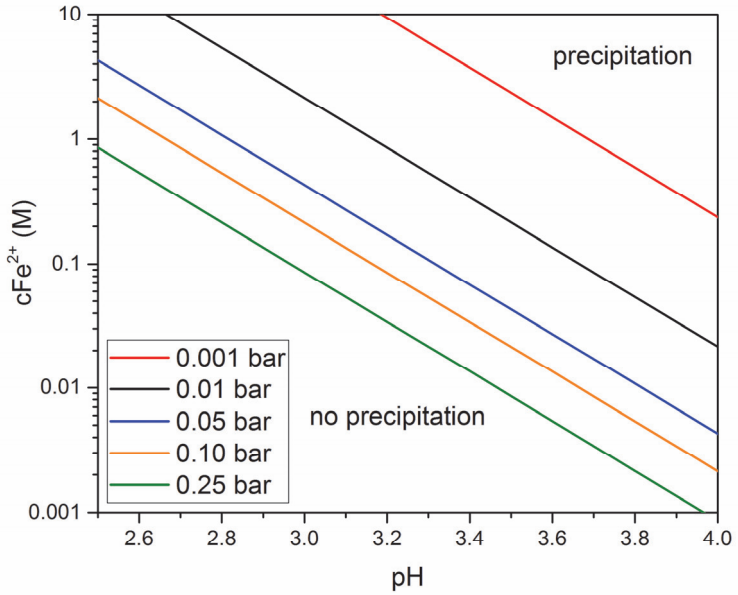

Figure 19: Calculated conditions for precipitation of FeS as a function of Fe^{2+} and pH for bulk H_2S concentrations equivalent to those used for the Phase 1 pitting tests at pH 4.0.

The significance of the FeS solubility highlights the criticality of the solution pH in a way that is quite different from its role in aerated systems. There is also a coherent rationale for the pit growth and related pit dependence on the H_2S concentration with an optimum H_2S concentration for pit growth just below or about the onset of precipitation. Also, too constrained a pit geometry would lead to a greater likelihood of precipitation so the pits that survive would tend to be more open than would be expected for stainless steel in aerated solution.

The results of the pitting tests performed in Phase 1 suggest that H_2S concentration influenced the mean and maximum pit size in both the well-buffered pH_{nom} 4.0 and weakly buffered pH_{nom} 4.5 solutions. Yet, in both cases the relationship was not monotonic, and the largest and most plentiful pits were observed at intermediate concentrations of H_2S, consistent with the solubility argument above. At pH_{nom} of 4.5, the most severe pitting was observed at H_2S partial pressures of 0.05 bar and 0.10 bar. At a pH_{nom} of 4.0, the most severe pitting was observed at H_2S partial pressures of 0.01 bar and 0.05 bar. This trend was more pronounced for the tests performed at the lower pH, which exhibited very small and few pits at the highest partial pressure of H_2S (0.25 bar). The tests in the lower pH solution also indicated larger pits for the low to intermediate H_2S concentrations suggesting that the expected more noble potential for the lower bulk solution pH was determining the dissolution kinetics, despite the greater buffering from the acetate ion. However, at higher concentrations of H_2S, pitting was more severe at pH_{nom} 4.5 compared to pH_{nom} 4.0. In this case it would appear that a lower pH was attainable in the pit with the less well buffered solution, which would increase the solubility of the metal sulphides.

A mechanistic process that could explain the results of Phase 1 can be summarised as follows.

The presence of a sufficient bulk concentration of H_2S will cause sulphidisation of the passive film, making it more permeable to chloride. The integration of chloride within the film will change its properties making it less passive and more vulnerable to localised corrosion. Passivation breakdown then occurs more readily, and the pit is maintained actively corroding by changes in chemistry in the pit coupled with adsorption of H_2S on the pit surface constraining the tendency to repassivation. This prevails at low H_2S concentrations but at higher concentrations, and as the pit grows, metal sulphides will precipitate within the pit, with the effect being more pronounced the less acidic the pit solution pH. At sufficiently high concentrations of H_2S, the precipitated metal sulphide will be dense enough to form a protective film on the pit surface and pitting will be inhibited. At slightly lower concentrations of H_2S, the precipitated metal sulphides will not form a dense protective film and will instead fill the pit with a porous precipitate. Pitting will continue to propagate underneath the precipitate.

5.2 MICROSTRUCTURAL EFFECTS

In the Phase I tests with the surface milled and ground, it was observed that the sides of the coupons suffered more severe pitting than the faces of the coupons (Figures 7 and 8). On the sides of the coupons, pits were both more abundant and larger than on the faces. The initiation of these pits may be attributed to the manufacturing process used to produce the coupons given that the corrosion resistance of 316L SS is heavily influenced by plastic deformation[26, 27], which has been shown to cause pit initiation in sour environments[3].

It had been specified that the sides of the coupon were to be produced to the same surface finish (0.2 µm Ra) as the faces, and that this should be achieved by a deep grinding process to remove 100 µm of material and hence remove the sub-surface deformation caused by the initial machining step.

Once initiated, the rapid growth of pits on the sides of the coupons can be explained with the aid of SEM cross-sections of the largest pits, which showed that pit growth was influenced by the steel microstructure. Transverse δ-ferrite stringers were visible in pits that initiated on the sides of coupons. When analysed by SEM-EDS, they were found to have chromium levels of ~26%, which is greater than the ~17% within the bulk and suggests that there would be associated chromium depletion in the austenite at the ferrite-austenite phase boundary. This is supported by the work of Sui et al. [28] who demonstrated that δ-ferrite present in 316L SS can sequester both Cr and Mo from the matrix to form a depleted zone, which under active corrosion leads to the formation of a micro-galvanic cell between the adjacent phases. Pits that initiated on the face of specimens (in plane with the rolling direction, see Figure 1) might not be expected to propagate along the phase boundaries to any significant depth due to the longitudinal orientation of the δ-ferrite (see Figure 2). However, previous work on the same batch of material, but in a high H_2S condensing environment, showed that deep pits that initiated at the

surface can propagate subsurface laterally by many millimeters[29], which presumably occurred when a pit intersected a δ-ferrite phase and propagated along the phase boundary between it and the matrix. The extent of this attack may have been specific to those environmental conditions, and perhaps would have been limited for the current high chloride test solutions, but the possibility that different sampling of material for the test coupons could induce such localised attack cannot be completely eliminated.

5.3 IMPACT OF SURFACE FINISH

The pitting tests undertaken in Phase 2, designed to characterise the evolution of pit depth with exposure time, were all performed in the testing environment that was shown to produce the most severe pitting in Phase 1, viz. 0.01 bar H_2S and pH_{nom} 4.0. However, the extent of pitting that was observed following each of the tests in Phase 2 was much less than was observed in Phase 1. Also, there was no correlation with exposure time of either the number of pits or their depth in the Phase 2 study, with an implication that pits may have initiated rapidly but propagation was not sustained.

Despite being prepared from the same batch of steel, the specimens exhibited very few pits exceeding 10 μm in depth, which was the threshold for detection in Phase 1. This is considered attributable to the difference in surface preparation between the specimens. In Phase 1, surfaces were mechanically ground using an automated grinding wheel to an Ra = 0.2 μm. Other than degreasing, no other surface preparation was performed prior to testing, which in some instance was many months after manufacture. In Phase 2, the specimens were ground using a manual grinding machine and SiC paper to a P1200 finish just prior to testing (Ra < 0.1 μm). This produced a much smoother and relatively defect free surface than was achieved in Phase 1.

Given that individual surface defects produced during automated surface grinding were identified as a significant pit precursor location for 316L SS when exposed to the same test conditions[3] it is not surprising that pitting was inhibited by the improved surface finish, noting the low S content of this steel. In the Phase 1 coupons there was significant sub-surface deformation and a high density of slip lines with depth of about 10 μm. The latter have been shown previously to enhance localised attack[3]. In the absence of these sensitive microstructural features the pit may have remained too shallow for the subsequent development to be self-sustaining.

The strong dependence of pitting on both microstructure and surface condition suggests that the difference in the pitting observed between each individual specimen is most likely dominated by the inherent variance in residual strain, grain orientation and prevalence of micro-mechanical defects. This is supported by the observation that within a single test, nominally identical test specimens exhibited pitting to varying degrees of severity, as has been reported in previous studies[29]. This demonstrates the difficulty of performing repeatable pitting tests on 316L SS and is due to its high sensitivity to mechanochemical effects[26].

In view of the tolerance in surface preparation allowed in NACE standards, for which only a requirement to achieve a sufficiently low Ra is often specified, this is a significant concern. There is a need for clearer specification of the surface finishing process, consideration of the use of hand-grinding in sensitive alloys such as 316L SS, and awareness of the potential significance of surface defects and near surface microstructural changes induced by the surface preparation method.

6 CONCLUSIONS

- Analysis of the passive film formed on 316L SS in simulated oilfield environment by nanoSIMS adds to the weight of evidence that sulphides in the film facilitate the permeation of chloride ions rendering the film susceptible to local breakdown.
- The influence of H_2S concentration on the subsequent pit propagation of 316L SS is non-monotonic with aggressivity being most significant at an intermediate concentration.

  - At low concentration of H_2S, pitting is observed, consistent with the proposition that adsorbed H_2S on the pit surface maintains an active surface, constraining the repassivation that might otherwise ensue in anoxic solution.
  - At intermediate concentration of H_2S, pitting is more severe, reflecting the higher concentration of free H_2S. Precipitation of metal sulphides may occur to some extent but the precipitate is assumed to be porous and not too restrictive to active corrosion.
  - At high concentration of H_2S, which might have been presumed to be most aggressive, pit development is significantly constrained, which is attributed to precipitation of protective dense sulphides limiting metal dissolution and easy access of H_2S. The growth of the pit is then stifled.
- The distinctive role of pH in the pit in this anoxic system is in determining the solubility of metal sulphides and the availability of free H_2S to adsorb on the reacting pit surface and sustain activity; the more acidic the pit solution the more soluble the iron sulphide and the greater impact of H_2S on pit propagation.
- The results of this study re-emphasise that pitting of 316L SS in sour oilfield brines is highly sensitive to surface condition. In that context, the specification of a maximum Ra value in stress corrosion cracking testing standards, for which pitting is often a precursor to cracking, is not sufficient to ensure a consistent surface finish and repeatability/reproducibility of pitting corrosion.

References

1. NACE MRO175/ISO 15156, Petroleum and gas industries - materials for use in H2S containing environments in oil and gas production (Houston, TX: NACE International).
2. Mat, S., Newman, R., Local chemistry aspects of hydrogen sulphide assisted SCC of stainless steel, Corrosion 1994, Paper no. 228, NACE Int., 1994.
3. G. Hinds, L. Wickström, K. Mingard, A. Turnbull, Impact of surface condition on sulphide stress corrosion cracking of 316L stainless steel, Corrosion Science 71, 43-52 (2013).
4. NACE TM0316-2016, Four-point bend testing of materials for oil and gas applications (Houston, TX: NACE International).
5. Hesketh, J., Cooling, P., Hinds, G., Validation of oxygen purge techniques for stress corrosion cracking tests, NPL Report, Mat 71, (2015).
6. Deng B, Jiang Y, Gong J, Zhong C, Gao, Li J, Critical pitting and repassivation temperatures for duplex stainless steel in chloride solutions, Electrochimica Acta, 53, 5220-5225, (2008).
7. Srinivasan J, Kelly R. G, Evaluating the Critical Chemistry for Repassivation at the Corroding Surface Using Mass Transport Model-Based Artificial Pit Experiments, Journal of the Electrochemical Society, 163, C768-C777, (2016).
8. Wang Z, Zhang L, Tang X, Zhang Z, Lu M, The surface characterization and passive behavior of Type 316L stainless steel in H2S-containing conditions, Applied Surface Science, 423, 457-464, (2017).
9. Wang Z, Zhang L, Zhang Z, Lu M, Combined effect of pH and H2S on the structure of passive film formed on type 316L stainless steel, Applied Surface Science, 458, 686-699, (2018).
10. Lee J.-S., Kitagawa Y., Nakanishi T., Hasegawa Y., Fushimi K. Effect of Hydrogen Sulfide Ions on the Passive Behavior of Type 316L Stainless Steel, Journal of the Electrochemical Society, 162, C685-C692, (2015).
11. Azuma S, Kudo T, Crevice Corrosion of Corrosion-Resistant Alloys in Simulated Sour Gas Environments, Corrosion, 47, 458-463, (1991).
12. Lei X, Wang H, Mao F, Zhang J, Zhao M, Fu A, et al, Electrochemical behaviour of martensitic stainless steel after immersion in a H_2S-saturated solution, Corrosion Science, 131, 164-173, (2018).
13. Hinds G, Wickström L, Abda J, Turnbull A, Smith V, Woollam R, Novel method for determination of pitting susceptibility in aggressive environments at elevated temperature and pressure, Corrosion Science, 85, 33-41, (2014).
14. Ilevbare G. O, Burstein G. T, The role of alloyed molybdenum in the inhibition of pitting corrosion in stainless steels, Corrosion Science, 43, 485-513, (2001).
15. Tomio A, Sagara M, Doi T, Amaya H, Otsuka N, Kudo T, Role of alloyed copper on corrosion resistance of austenitic stainless steel in H_2S–Cl^- environment, Corrosion Science, 81, 144-151, (2014).
16. Azuma S, Tsuge H, Kudo T, Moroishi T, Crevice Corrosion of Duplex Stainless Steel in Simulated Sour Gas Environments, Corrosion, 45, 235-242, (1989).
17. Pou T. E, Murphy O. J, Young V, Bockris J. O. M, Tongson L. L, Passive Films on Iron: The Mechanism of Breakdown in Chloride Containing Solutions, Journal of the Electrochemical Society, 131, 1243-1251, (1984).
18. Bernard F, Rao V. S, Kwon H.-S, A Study on the Repassivation Kinetics and SCC Behavior of Duplex Stainless Steel in Chloride Solution, Journal of the Electrochemical Society, 152, B415-B420, (2005).
19. Mattin S. P, Burstein G. T, Detailed resolution of microscopic depassivation events on stainless steel in chloride solution leading to pitting, Philosophical Magazine Letters, 76, 341-348, (1997).
20. Fushimi K, Takakura K.-H, Habazaki H, Konno H, Azumi K, Tsuri S, Depassivation pH of Austenitic Stainless Steels in NaCl Aqueous Solution, ECS Transactions, 16, 291-296, (2009).
21. Frankel G. S, Pitting Corrosion of Metals: A Review of the Critical Factors, Journal of the Electrochemical Society, 145, 2186-2198, (1998).

22. Ravindranath K, Al-Wakaa B, Tanoli N, Shalaby H. M. The Effect of Chloride-Hydrogen Sulfide Synergism on the Stress Corrosion Cracking Susceptibility of Type 321 Stainless Steel, Corrosion, 73, 1268-1279, (2017).
23. A. Kahyarian, S. Nesic, H_2S corrosion of mild steel: A quantitative analysis of the mechanism of the cathodic reaction, Electrochimica Acta, 297 (2019) 676-684.
24. Hesketh, J., Dickinson E., McMahon, G., Turnbull, A., Hinds, G., Influence of H_2S on the localised corrosion of 316L stainless steel Part 2 – Electrochemcial testing, NPL Report MAT 94, (2020).
25. van Haaften, W.M., pers. comm., Shell Amsterdam, 2020.
26. Gutman E. M, Solovioff G, Eliezer D, The mechanochemical behavior of type 316L stainless steel, Corrosion Science, 38, 1141-1145, (1996).
27. Wu G, Singh M. P, Effect of Plastic Deformation on Pitting Mechanism of SS304, Metallurgical and Materials Transactions A, Volume 50, 4750-4757, (2019).
28. Sui G, Charles E. A, Congleton J, The effect of delta-ferrite content on the stress corrosion cracking of austenitic stainless steels in a sulphate solution, Corrosion Science, 38, 687-703, (1996).
29. Hinds G, Turnbull A, Hesketh J, Role of H_2S in Localized Corrosion and Cracking of CRAs in Upstream Oil and Gas Applications, Corrosion 2017, NACE International, (2017).